Electronic Supplementary Material (ESI) for Journal of Materials Chemistry A.

Structural dynamics of Schottky and Frenkel defects in ThO_2: a density-functional theory study - supporting information

Samuel Moxon,[¥] Jonathan Skelton,[†,*] Joshua S. Tse,[¥] Joseph Flitcroft,[¥,†] A. Togo,[§] David J. Cooke,[¥] E. Lora da Silva,[‡] Robert M. Harker,[⁋] Mark T. Storr,[⁋] Stephen C. Parker,[£] and Marco Molinari[¥,*]

[¥] *Department of Chemical Sciences, University of Huddersfield, Queensgate, Huddersfield, HD1 3DH*
[†] *Department of Chemistry, University of Manchester, Manchester M13 9PL, UK*
[‡] *IFIMUP, Department of Physics and Astronomy, Faculty of Science, University of Porto, 4169-007 Porto, Portugal*
[§] *National Institute for Materials Science (NIMS), 1-2-1 Sengen, Tsukuba-city, Ibaraki 305-0047, Japan*
[⁋] *AWE Aldermaston, Reading, RG7 4PR, UK*
[£] *Department of Chemistry, University of Bath, Claverton Down, Bath, BA2 7AY, UK*
* Corresponding authors: *m.molinari@hud.ac.uk* and *jonathan.skelton@manchester.ac.uk*

As noted in the text, we considered two methods for calculating the defect formation free energies ΔA_f, *viz.* Methods 1 and Method 2. In both cases, we calculate the Helmholtz energy of a given system according to:

$$A(T) = U_0 + A_{vib}(T) = U_0 + U_{vib}(T) - TS_{vib}(T) \quad (1)$$

The main difference is that in Method 2 we only take into account the frequencies at the Γ-point, as opposed to interpolating frequencies and integrating over the Brillouin zone (BZ) as in Method 1. This is a common approximation, and is useful in high throughput screening of materials and defects as it reduces the computational demand of the calculations. Moreover, since computing the force constants in a single (defect) cell formally only allows the Γ-point frequencies to be evaluated exactly, for practical defect supercells integrating over the BZ will require Fourier interpolation, which is itself an approximation.

One of the issues with Method 1 is that at the Γ-point the three acoustic modes correspond to rigid translations with zero frequency, whereas away from Γ they tend to be low-frequency modes and heavily populated at finite temperature, and therefore to make a large contribution to the vibrational partition function. This is usually dealt with through one of three approximations as follows.

(1) Approximation 1: the low-temperature limit. We assume the translation modes do not contribute to the energy of the phonon system, and the vibrational free energy is computed based on the frequencies of the other 3^{n_a} - 3 Γ-point modes.

The vibrational internal energy is given by:

$$U_{vib}(T) = \sum_i^{3n_a} R\theta_i \left[\frac{1}{2} + \frac{1}{exp(\theta_i/T) - 1}\right] = U_{ZPE} + \sum_i^{3n_a} \frac{R\theta_i}{exp(\theta_i/T) - 1} \quad (2)$$

where U_{ZPE} is the vibrational zero-point energy and the sums run over the 3^{n_a} vibrational modes with frequencies ν_i and the characteristic vibrational temperatures θ_i given by:

$$\theta_i = \frac{h\nu_i}{k_B} \quad (3)$$

The S_{vib} is calculated as:

$$S_{vib}(T) = \frac{U_{vib}(T) - A_{vib}(T)}{T} \quad (4)$$

where A_{vib} is the vibrational Helmholtz free energy:

$$A_{vib}(T) = U_{ZPE} + \sum_i^{3n_a} RTln\left(1 - exp\left[\frac{-\theta_i}{T}\right]\right) \quad (5)$$

(2) Approximation 2: the high-temperature (Dulong-Petit) limit. We assume that each translational mode has a constant modal heat capacity $C = R$ and therefore that the U_{vib}^{t} associated with the three translational modes is:

$$U_{vib}^{t}(T) = 3 \times \int C_v dT = 3 \times \int R dT = 3RT \quad (6)$$

The corresponding vibrational entropy S_{vib}^{t} is given by:

$$S_{vib}^{t}(T) = \int \frac{C_v}{T} dT = 3R \int \frac{1}{T} dT = 3Rln(T) \quad (7)$$

The additional contributions from Eqns. S6 and S7 can then be added to Eqns. S2 and S4, respectively.

(3) Approximation 3. Since we work with a supercell and expect some degree of band folding, we assume that the three lowest-energy modes with non-zero frequency are folded zone-boundary acoustic modes from the parent primitive cell. We further assume a linear dispersion from zero at the zone centre. Thus, we can approximate that the first 3 modes to contribute to U_{vib} and S_{vib}, would assume values that are the midpoint between 0 THz and the three lowest-energy modes with non-zero frequency. Once determined, these frequencies can be used to replace the zero-frequency acoustic modes in Approximation 1.

Fig. S1 compares the calculated defect-formation free energies as a function of temperature for the ThF<111>, OF<113>, S<100>, S<110> and S<111> defects computed using Method 1, as in the text, and Method 2 with Approximations 1-3. As noted in the text, there is some small variation in the temperature dependence from the four sets of predictions, by up to ~0.25-0.5 eV at T = 3600 K, but the qualitative stability ordering remains unchanged.

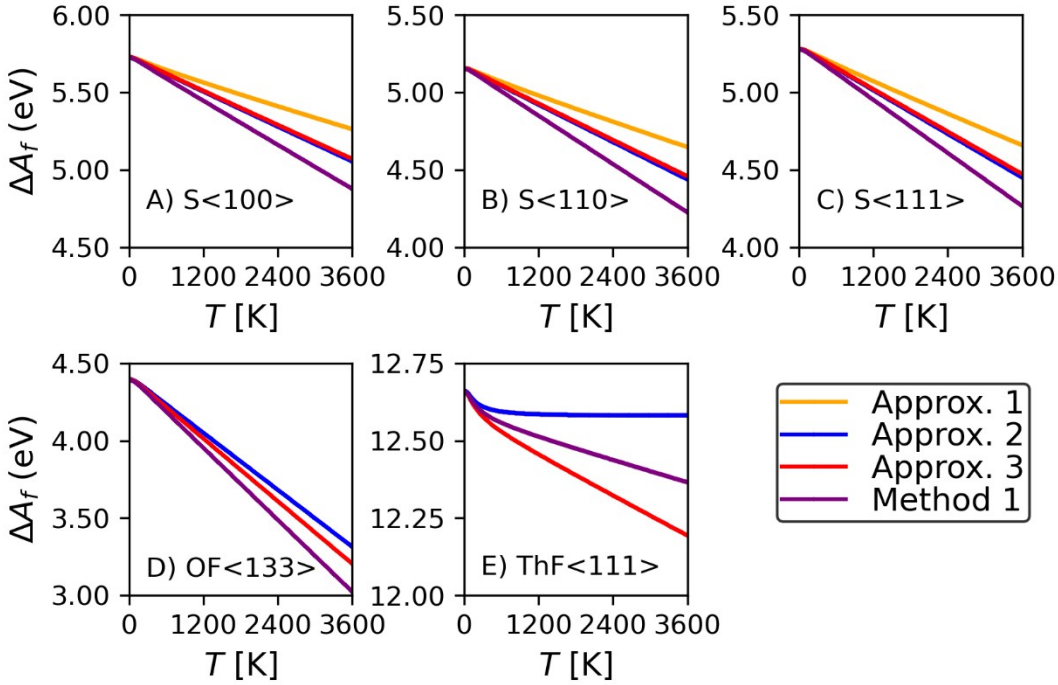

Figure S1 Defect-formation free energies for the S<100> (A), S<110> (B), S<111> (C), OF<133> (D) and ThF<111> (E) defects calculated using Method 2 with Approximations 1-3 and compared to the results form Method 1 shown in the main paper. Note that in (D) and (E) Approximations 1 and 2 produce very similar results and the corresponding lines thus overlap with one another.

The absolute infrared activity of a Γ-point mode with band index s is calculated as:[1–3]

$$I_{IR}(s) = \sum_{\alpha=1}^{3} \left| \sum_{j=1}^{n_a} \sum_{\beta=1}^{3} Z_{\alpha\beta}^{*}(j) X_{\beta}(s,j) \right|^2 \quad (8)$$

where the indices α and β label the Cartesian directions, $Z^*(j)$ are the Born effective-charge tensors of the jth atom, and $X(s,j)$ are the cartesian displacements of atom j for the band index s obtained by dividing the eigenvector components $W(s,j)$ by the square root of the corresponding atomic mass m_j.

The Raman activity tensors for the modes are computed as the derivative of the high-frequency dielectric constant ε^{∞} with respect to the normal mode amplitude $Q(s)$ using the central difference scheme:[3,4]

$$I_{Raman,\alpha\beta}(s) = \frac{\Omega}{4\pi}\left[-\frac{1\varepsilon^{\infty}_{\alpha\beta}(-s)}{2\ \Delta Q(s)} + \frac{1\epsilon^{\infty}_{\alpha\beta}(+s)}{2\ \Delta Q(s)}\right] \tag{9}$$

where Ω is the unit-cell volume. The Raman intensity measured in an experiment depends on the direction and polarisation of the exciting radiation and the collection direction and polarisation of the analyser. We assume a powder sample and compute the scalar average of the Raman tensor according to:[2,3]

$$I_{Raman} = 45\left|\frac{1}{3}(I_{11}+I_{22}+I_{33})\right|^2 + \frac{7}{2}\left[(I_{11}-I_{22})^2 + (I_{11}-I_{33})^2 + (I_{22}-I_{33})^2 + 6\left({I_{12}}^2 + {I_{13}}^2 + {I_{23}}^2\right)\right] \tag{10}$$

where $I_{\alpha\beta}$ are the components of the Raman tensor.

IR and Raman spectra are modelled as a sum of the spectral lines from each of the 3^{n_a} Γ-point modes. We assume a Lorentzian lineshape with the central frequencies and areas set to the calculated phonon frequencies and IR/Raman activities (Eqn. 8 and 10), such that the combined spectral intensity at a frequency v and temperature T is given by:

$$I(v,T) = \sum_s \frac{I(s)}{\pi} \frac{\frac{1}{2}\Gamma(s,T)}{(v-v(s))^2 + \left(\frac{1}{2}\Gamma(s,T)\right)^2} \tag{11}$$

The linewidths $\Gamma(s,T)$ may be set to a constant or can be extracted from the third-order phonon calculations. In the latter case they are related to the temperature-dependent phonon lifetimes $\tau(s,T)$ according to:

$$\tau(s,T) = \frac{1}{2\Gamma(s,T)} \tag{12}$$

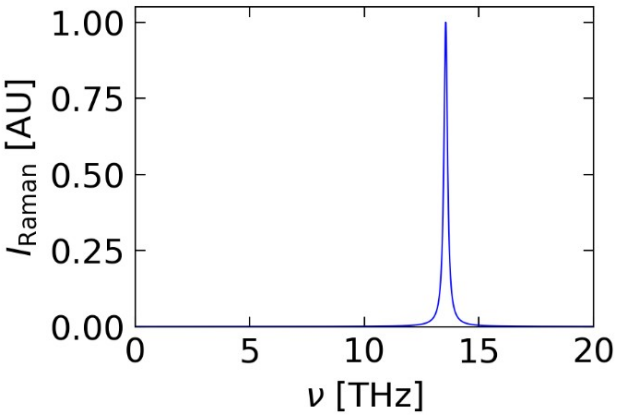

Figure S2 Simulated Raman spectrum of stoichiometric ThO_2 using the calculated T = 600 K linewidth of Γ = 0.186 THz.

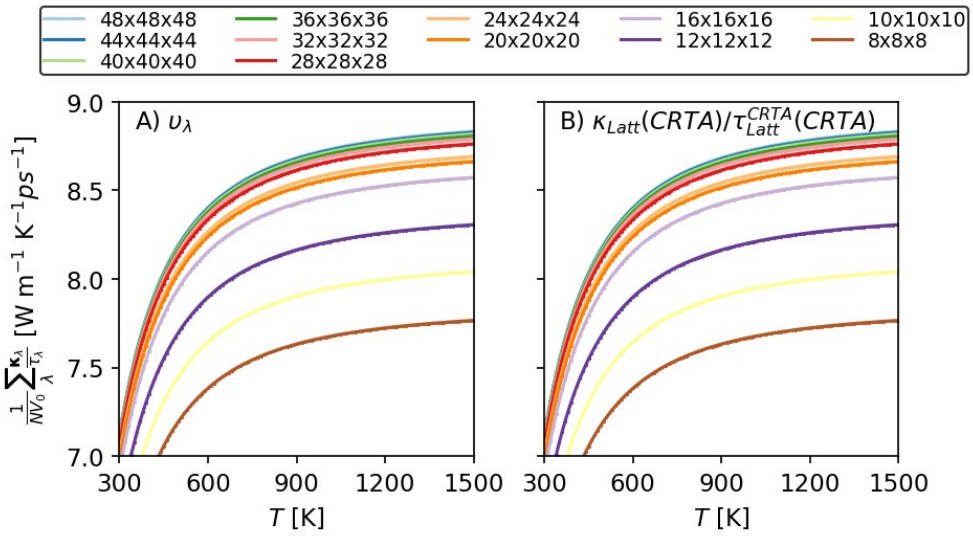

Figure S3 Convergence of the harmonic function defined in Eqn. 16 in the text for the ThO_2 primitice cell as a function of the q-point sampling mesh. The curves in (A) and (B) are identical.

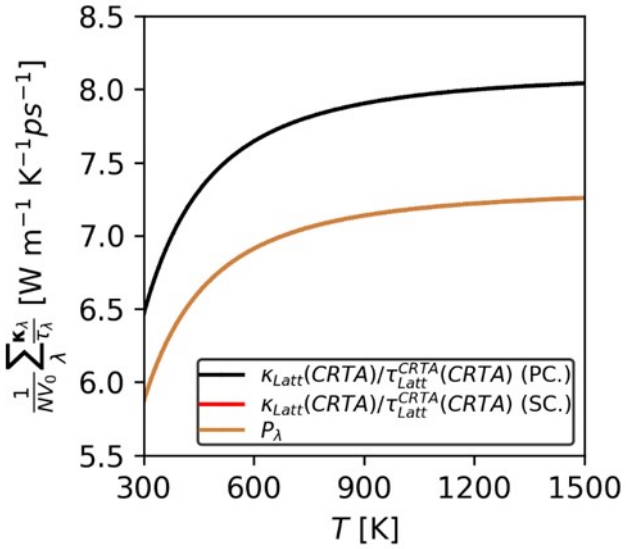

Figure S4 Comparison of the harmonic function defined in Eqn. 16 in the text computed for the ThO_2 primitive cell with a 48 × 48 × 48 q-point sampling mesh and the 96-atom supercell used for the defect models with a 10 × 10 × 10 mesh. The red and orange curve overlap.

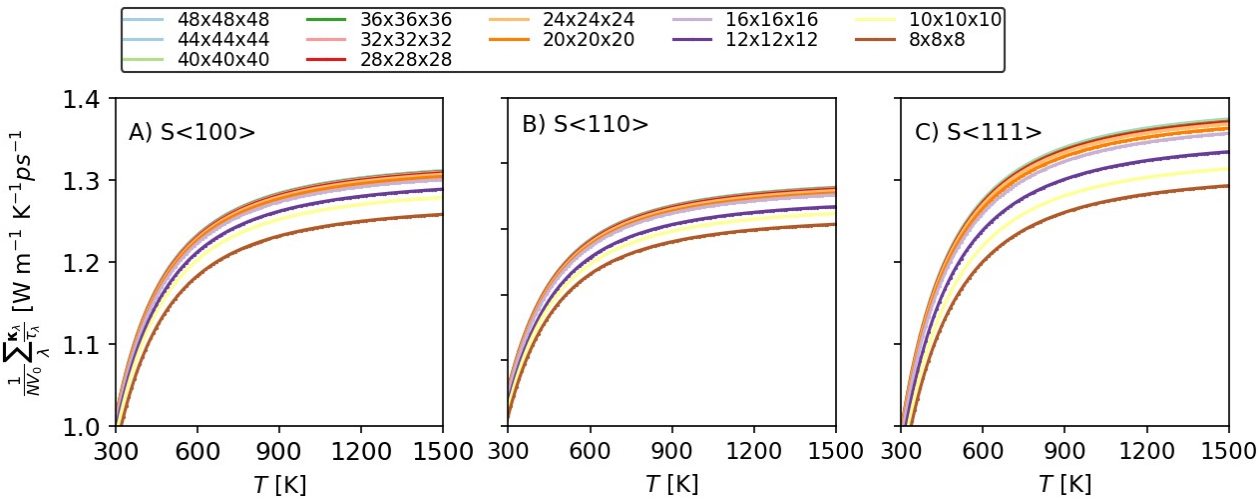

Figure S5 Convergence of the harmonic function defined in Eqn. 16 in the text for the S<100>, S<110> and S<111> defect models as a function of the q-point sampling mesh.

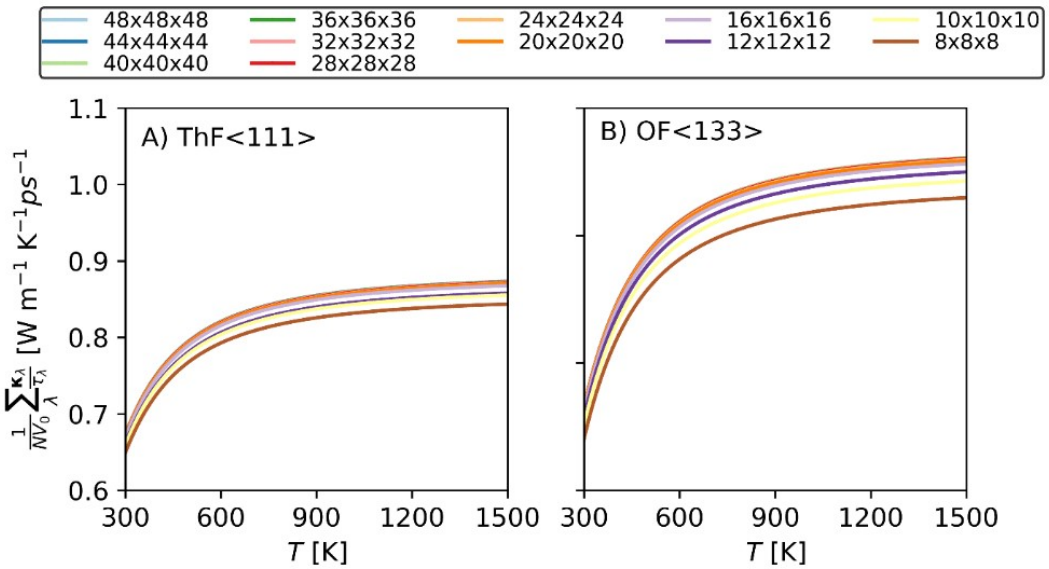

Figure S6 Convergence of the harmonic function defined in Eqn. 16 in the text for the Th<111> and OF<133> defect models as a function of the q-point sampling mesh.

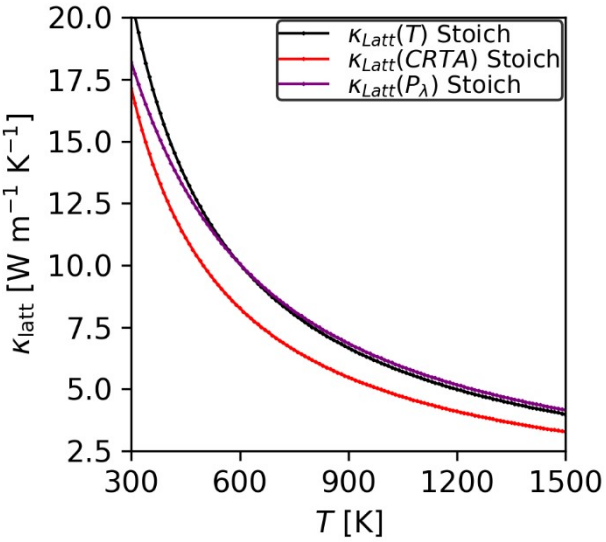

Figure S7 Comparison of the thermal conductivity of stoichiometric ThO_2 computed using three methods: (1) for the primitive cell using Eqn. 11; (2) for the 96-atom supercell using the CRTA model in Eqn. 16 with the τ^{CRTA} computed for the primitive cell; and (3) for the supercell using the constant P_λ model with $the\ P$ fitted to reproduce the κ_{latt} of the primitive cell at T = 600 K (Eqns. 11, 14 and 19 in main manuscript).

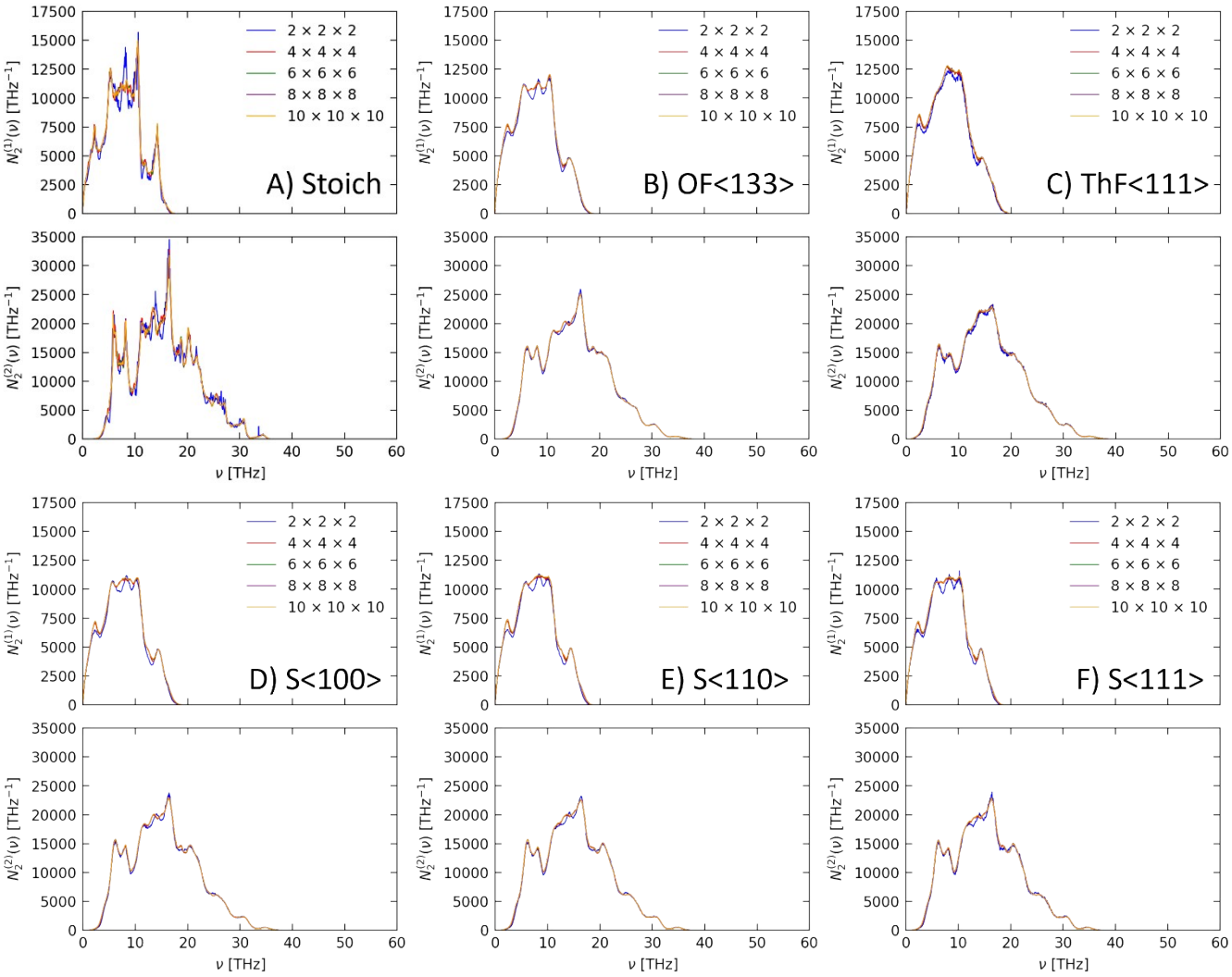

Figure S8 Convergence of the weighted joint density of states (wJDOS) function $\bar{N}_2(\omega) = \bar{N}_2^{(1)}(\omega) + \bar{N}_2^{(2)}(\omega)$ defined in Eqn. 24 in the text for the stoichiometric 96-atom ThO_2 supercell (A) and the OF<133> (B), ThF<111> (C), S<100> (D), S<110> (E) and S<111> (F) defect models as a function of the q-point sampling mesh. Each pair of subplots shows the convergence separately for the component $\bar{N}_2^{(1)}$ and $\bar{N}_2^{(2)}$ functions.

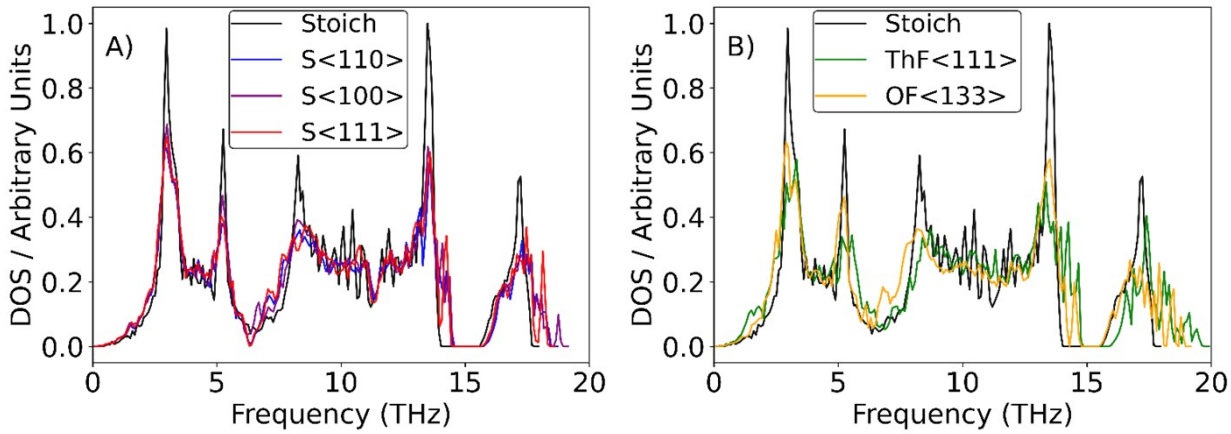

Figure S9 Comparison of the phonon density of states (DOS) of stoichiometric ThO_2 (black) to (1) the S<100>, S<110> and S<111> Schottky defects (blue, purple, red), and (B) the OF<133> and ThF<111> Frenkel defects (green, orange).

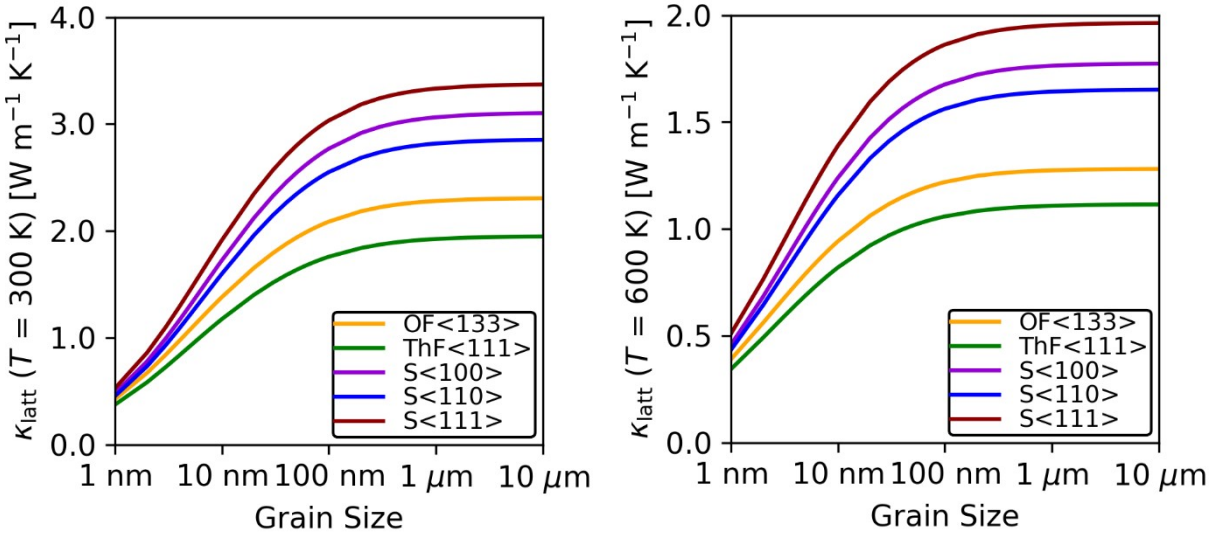

Figure S10 Estimated thermal conductivity of the five defect models considered in this work at T = 300K (left) and T = 600K (right) as a function of crystal-grain size, computed using a boundary-scattering model and using the constant-P_λ model outlined in the text.

References

1 D. Karhánek, T. Bučcko and J. Hafner, *J. Phys. Condens. Matter*, 2010, **22**, 265005.

2 D. Porezag and M. R. Pederson, *Phys. Rev. B*, 1996, **54**, 7830.

3 J. M. Skelton, L. A. Burton, A. J. Jackson, F. Oba, S. C. Parker and A. Walsh, *Phys. Chem. Chem. Phys.*, 2017, **19**, 12452–12465.

4 A. Fonari and S. Stauffer, *vasp_raman.py*, https://github.com/raman-sc/VASP/, 2013.